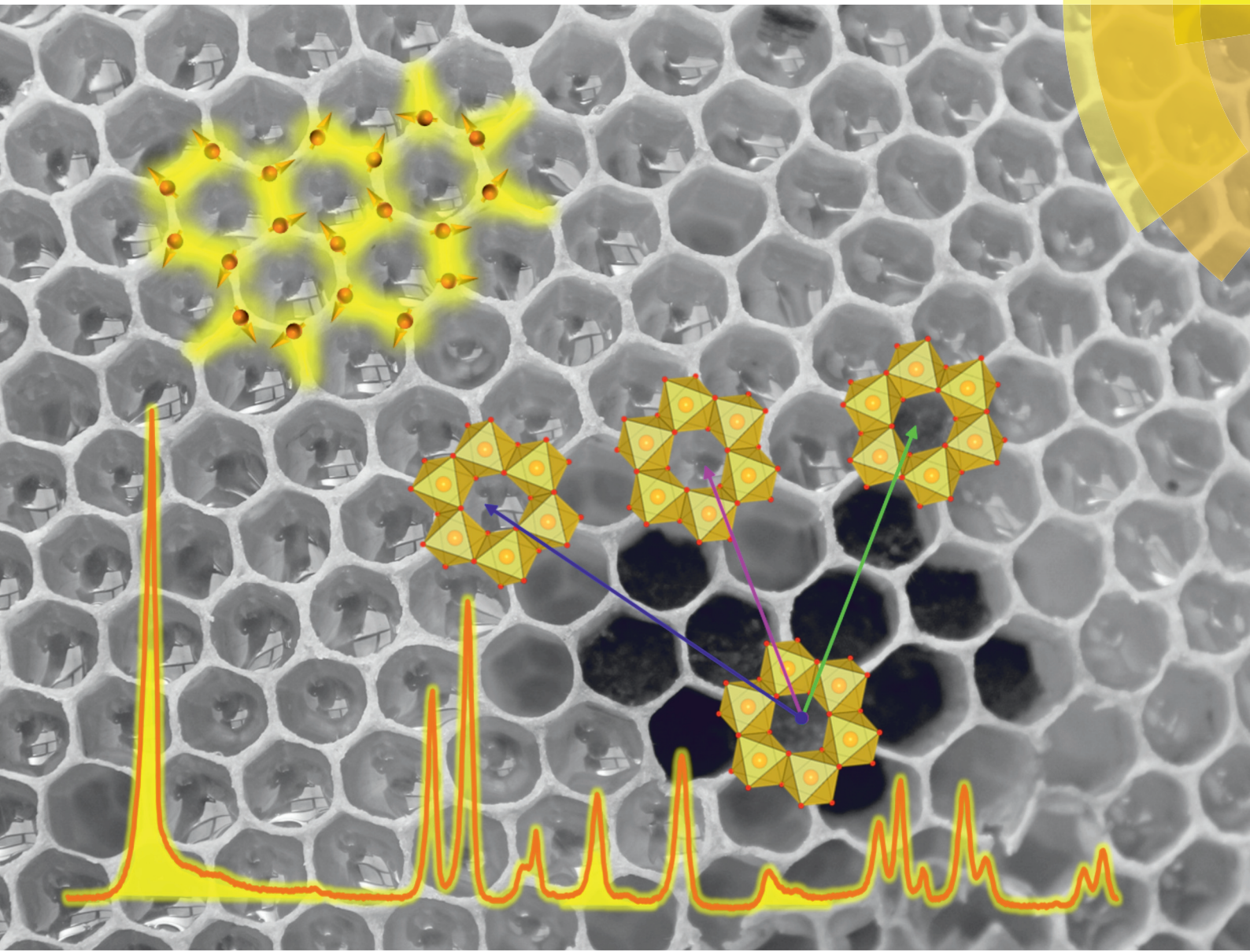


Dalton Transactions

An international journal of inorganic chemistry

rsc.li/dalton



ISSN 1477-9226



PAPER

Sebastian Bette *et al.*

Solution of the heavily stacking faulted crystal structure of the honeycomb iridate $H_3LiIr_2O_6$



Cite this: *Dalton Trans.*, 2017, **46**, 15216



Solution of the heavily stacking faulted crystal structure of the honeycomb iridate $H_3LiIr_2O_6$ †

Sebastian Bette, *^a Tomohiro Takayama, ^a Kentaro Kitagawa, ^b Riku Takano, ^b Hidenori Takagi^a and Robert E. Dinnebier ^a

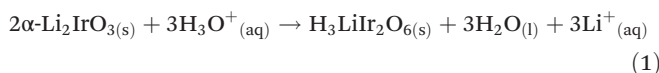
A powder sample of pure $H_3LiIr_2O_6$ was synthesized from α - Li_2IrO_3 powder by a soft chemical replacement of Li^+ with H^+ . The crystal structure of $H_3LiIr_2O_6$ consists of sheets of edge sharing LiO_6^- and IrO_6^- octahedra forming a honeycomb network with layers stacked in a monoclinic distorted $HCrO_2$ type pattern. Heavy stacking faulting of the sheets is indicated by anisotropic peak broadening in the X-ray powder diffraction (XRPD) pattern. The ideal, faultless crystal structure was obtained by a Rietveld refinement of the laboratory XRPD pattern while using the $LiIr_2O_6^{3-}$ -layers of α - Li_2IrO_3 as a starting model. The low radial distances of the PDF function, derived from synchrotron XRPD data, as constraints to stabilize the structural refinement. DIFFaX-simulations, structural considerations, high radial distances of the PDF function and a Rietveld compatible global optimization of a supercell were employed to derive a suitable faulting model and to refine the microstructure using the experimental data. We assumed that the overall stacking pattern of the layers in the structure of $H_3LiIr_2O_6$ is governed by interlayer O–H...O contacts. From the constitution of the layers, different stacking patterns with similar amounts of strong O–H...O contacts are considered. Random transitions among these stacking patterns can occur as faults in the crystal structure of $H_3LiIr_2O_6$, which quantitatively describe the observed XRPD.

Received 11th August 2017,
 Accepted 23rd September 2017

DOI: 10.1039/c7dt02978k
 rsc.li/dalton

Introduction

$H_3LiIr_2O_6$ is a layered double hydroxide oxide salt, hence the formula can be expressed alternatively as $LiIr_2O_3(OH)_3$. The compound was recently revealed to be the pH sensing phase in an IrO_x -based solid state electrode.¹ The pH electrode is a promising supplement for glass electrodes, as thin glass membranes are incompatible with high pressures and temperatures, as well as with extreme alkaline and hydrofluoric media.^{2–4} IrO_x -based solid state electrodes can be produced by the carbonate melt oxidation process^{5–7} in which iridium wires are oxidized in an excess of molten lithium carbonate. This process leads to the formation of α - Li_2IrO_3 .^{1,8} In a subsequent step the excess of lithium carbonate is dissolved by acid treatment and α - Li_2IrO_3 is transformed into $H_3LiIr_2O_6$ by cation exchange (eqn (1)).



Profound crystallographic knowledge of the α - Li_2IrO_3 – $H_3LiIr_2O_6$ system is essential for understanding and controlling the process presented in (eqn (1)) and in consequence also for the production of stable and reliable pH sensing IrO_x -based solid state electrodes.

The crystal structure of α - Li_2IrO_3 was determined from X-ray powder diffraction (XRPD) data.⁹ It consists of layers of edge sharing IrO_6^- and LiO_6^- octahedra and lithium ions that are situated in the interlayer spacing (Fig. 1, left). Accordingly

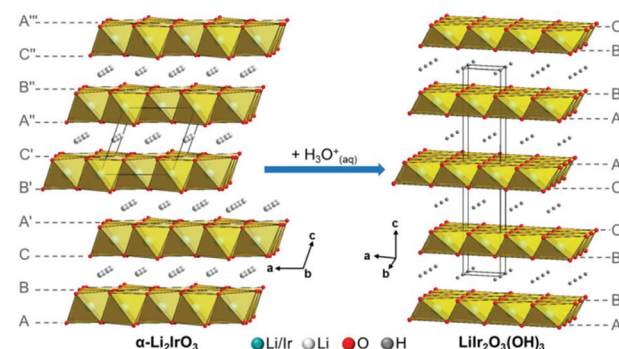


Fig. 1 Packing diagram in the crystal structure of α - Li_2IrO_3 (left) that can be transformed into $LiIr_2O_3(OH)_3$ (packing diagram, right) by acid treatment. The stacking order of the anion sublattice is indicated by capital Latin letters.

^aMax Planck Institute for Solid State Research, Heisenbergstr. 1, 70569 Stuttgart, Germany. E-mail: S.Bette@fkf.mpg.de

^bDepartment of Physics, University of Tokyo, 7-3-1 Hongo, Tokyo 113-0033, Japan

† Electronic supplementary information (ESI) available. See DOI: 10.1039/c7dt02978k

the formula can be alternatively written as $\text{Li}_3^{\text{I}}\text{Li}^{\text{II}}\text{Ir}_2^{\text{II}}\text{O}_6$ with atoms situated in the interlayer space indicated by “I” and atoms within the layers indicated by “II”. O’Malley *et al.*⁹ observed the occurrence of stacking faults in the crystal structure of $\alpha\text{-Li}_2\text{IrO}_3$, which is a common phenomenon in layered alkali- and earth alkali metal iridates.^{10,11} Hence the slight occupational disorder between Li^+ and Ir^{4+} in the layers, which was introduced to the structural model during the refinement, could be an artefact from daubed reflection intensities due to diffraction line broadening by the appearance of stacking faults.^{10,11} The overall structural motif of $\alpha\text{-Li}_2\text{IrO}_3$ is closely related, but not identical to LiCoO_2 .¹² Due to the honeycomb ordering of the 2 Ir-sites and the Li-site within the layer of Li_2IrO_3 and the associated monoclinic distortion of the unit cell of $\alpha\text{-Li}_2\text{IrO}_3$ the anion sublattice exhibits an ABCA’B’C’A”B”C”..., stacking (Fig. 1, left), with anion positions indicated by capital Latin letters, that slight differs from the ABC anion stacking pattern in the structure of LiCoO_2 .

By acid treatment only the lithium ions situated in-between the layers are exchanged by protons which lead to the formation of $\text{H}_3\text{LiIr}_2\text{O}_6$ (Fig. 1, right). The occurrence of stacking faults in $\alpha\text{-Li}_2\text{IrO}_3$ is crucial for the production of $\text{H}_3\text{LiIr}_2\text{O}_6$, as the degree of cation exchange is the higher, the higher the degree of faulting of the precursor material.¹ O’Malley *et al.*¹ expected $\text{H}_3\text{LiIr}_2\text{O}_6$ to crystallize in a HCrO_2 like structure with an AABBCC stacking pattern of the anion sublattice, where oxygen sites of neighbouring layers directly oppose each other, which results in strong H-bonds. Because of the pronounced occurrence of stacking faults they only determined a rough estimate of the crystal structure. Neither the exact type nor the degree of stacking faulting in the $\text{H}_3\text{LiIr}_2\text{O}_6$ structure, which has an impact of the pH sensing properties,¹ has been understood, yet.

$\text{H}_3\text{LiIr}_2\text{O}_6$ attracts considerable attention not only as PH sensor materials but as a promising candidate for a topological quantum spin liquid described by Kitaev model.¹³ In particular iridates with a honeycomb like structural motif, like $\alpha\text{-Li}_2\text{IrO}_3$ ⁹ and $\beta\text{-Li}_2\text{IrO}_3$ ¹⁴ are promising candidates for the materialization of the Kitaev model. In a honeycomb lattice strong spin frustration effects stabilize a quantum spin liquid state, in which novel excitations, like Majorana fermions and fluxes are apparent.¹⁵ $\alpha\text{-Na}_2\text{IrO}_3$ ¹⁶ and $\alpha\text{-Li}_2\text{IrO}_3$ ¹⁷⁻²¹ were first expected to be a materialization of Kitaev model but a magnetically ordered state was found to be the ground state of the two honeycomb iridium oxides. $\text{H}_3\text{LiIr}_2\text{O}_6$, a modified honeycomb iridate, was visited as an alternative candidate and was discovered not to show any magnetic ordering down to 1 K.²² This is indicative for the realization of a spin liquid as the ground state. To clarify the reason why quantum spin liquid can be stabilized in $\text{H}_3\text{LiIr}_2\text{O}_6$, a detailed structural understanding, including the microstructural effects like stacking faults, is necessary.

In the current study, we re-evaluate the structure model of $\text{H}_3\text{LiIr}_2\text{O}_6$ given by O’Malley *et al.*¹ and after we show that this model is not suitable, we describe the redetermination of the ideal crystal structure of $\text{H}_3\text{LiIr}_2\text{O}_6$ by using XRPD data and

PDF-analysis. As the XRPD data indicate a strongly stacking faulted crystal lattice, possible structural defects are derived from the crystal structure and investigated by systematic DIFFaX simulations. A Rietveld compatible approach was used to determine the real structure, *i.e.* the degree of faulting by using a supercell approach. The obtained superstructure is confirmed by PDF-analysis. The approach used in this study should pave a way to determine the crystal structure and the degree of stacking faulting of the layered materials of interest.

Experimental section

Synthesis of $\text{H}_3\text{LiIr}_2\text{O}_6$

$\text{H}_3\text{LiIr}_2\text{O}_6$ was synthesized by using an $\alpha\text{-Li}_2\text{IrO}_3$ precursor. The precursor was obtained by a solid state reaction of Li_2CO_3 (Chempur, 99.995%) and IrO_2 (Tanaka Kikinzoku Kogyo, 86 wt% Ir) in which a 5% excess of Li_2CO_3 was added to the stoichiometric mixture in order to compensate for volatilization of Li at high temperatures. Tempering of the mixture was conducted at 1000 °C for 24 h. During that period the powder was ground twice to provide a sufficient mixing. Afterwards the mixture was cooled down to room temperature in the oven. The obtained powder was confirmed to be a single phase of $\alpha\text{-Li}_2\text{IrO}_3$ by laboratory XRPD. For cation exchange the $\alpha\text{-Li}_2\text{IrO}_3$ powder was placed in a Teflon-lined steel autoclave and 4 mol L⁻¹ H_2SO_4 aqueous solution was added. The mixture was heated in the sealed vessel at 120 °C for 96 hours. Afterwards the product was washed with distilled water and dried at room temperature. The obtained powder is insensitive against air.

Solid phase characterization

Laboratory X-ray powder diffraction (XRPD). The XRPD-pattern of the solid phase was collected at room temperature on a laboratory powder diffractometer in Debye–Scherrer geometry (Stadi P-Diffractometer (Stoe), Ag-K_{α1} radiation from primary Ge(111)-Johann-type monochromator, Mythen 1 K detector (Dectris)). The sample was sealed in a 0.5 mm diameter borosilicate glass capillary (Hilgenberg glass no. 14), which was spun during the measurement.

Synchrotron X-ray powder diffraction. Synchrotron X-ray total scattering pattern of the sample was recorded in Debye–Scherrer mode at the National Synchrotron Light Source (NSLS), Brookhaven National Laboratory, at a wavelength of $\lambda = 0.1847$ Å (67.13 keV) on beamline X28B1 equipped with a Si(311) sagittal focusing double Laue crystal monochromator. Diffracted X-rays were detected using a PerkinElmer detector (2048 × 2048 pixels and 200 × 200 μm^2 pixel size) mounted orthogonal to the beam path with a sample-to-detector distance of 205.80 mm. The measured samples were sealed in kapton tubes of 1.0 mm diameter. The collected Debye–Scherrer rings were subsequently azimuthally integrated with the program FIT2D²³ to one-dimensional powder diffraction patterns in Q [nm^{-1}] and 2θ [°] versus intensity. Parameters for intensity integration were determined from a LaB_6 reference

sample. Using the software TOPAS,²⁴ Rietveld refinements²⁵ were carried out, applying the fundamental parameter method^{26,27} for peak modelling and Chebyshev polynomials for modelling the background.

Pair distribution function (PDF) analyses. PDFGETX2²⁸ was used to correct and normalize the diffraction data and the Fourier transform in order to obtain the experimental PDF, $G(r)$. The Q range used in the Fourier transform was limited to 30 \AA^{-1} . Nickel was previously measured as a standard material to determine the Q -damp and Q -broad parameters which are the parameters that correct the PDF envelope function for instrumental resolution effects.^{29,30} For structural modelling TOPAS 6.0³¹ was used. Atomic positions of the compounds under investigation were taken from the corresponding structural models presented here and from the assumed crystal structure of $\text{H}_3\text{LiIr}_2\text{O}_6$ of O'Malley *et al.*¹ However, certain parameters were adjusted to improve the agreement. These were scale factor, Q -damp, Q -broad, the two trigonal lattice parameters and an overall isotropic displacement parameter.

Results and discussion

Crystal structure solution

Evaluation of the HCrO_2 -like structure model. The measured XRPD pattern of the synthesized $\text{H}_3\text{LiIr}_2\text{O}_6$ appeared to be very similar to the reported pattern of O'Malley *et al.*¹ Accordingly, in a first attempt the trigonal HCrO_2 like crystal structure model of $\text{H}_3\text{LiIr}_2\text{O}_6$ which was created by them was used as a starting model for a Rietveld refinement²⁵ of the measured diffraction pattern using the program TOPAS 6.0.³¹ This procedure, however, led to an insufficient fit as several sharp peaks couldn't be described by the crystal structure model (Fig. 2, green circles). The misfit of the reflection intensities is most likely caused by the insufficient modelling of peak broadening, which is caused by the pronounced occurrence of stacking faults. This indicates that the $R\bar{3}m1$ space group symmetry, as well as the unit cell of the predicted crystal structure is not suitable.

In addition, in the trigonal HCrO_2 like structure model the cation sublattice is completely occupationally disordered between lithium and iridium and all oxygen sites are situated

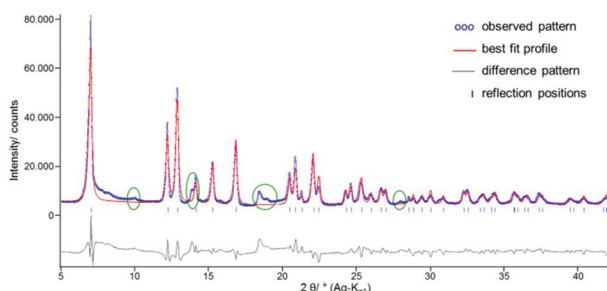


Fig. 2 Excerpt of the final Rietveld refinement of diffraction pattern of $\text{H}_3\text{LiIr}_2\text{O}_6$ using the predicted crystal structure by O'Malley *et al.*¹ as starting model.

on an identical plane. If this model was appropriate, the cation exchange by acid treatment would have caused a vast change in the constitution of the layers. The solid-state NMR data, however, point to an ordered cation sublattice (ESI, Fig. S1†).

Derivation of the idealized, faultless crystal structure of $\text{H}_3\text{LiIr}_2\text{O}_6$. As $\text{H}_3\text{LiIr}_2\text{O}_6$ was produced by cation exchange *via* acid treatment of $\alpha\text{-Li}_2\text{IrO}_3$ (eqn (1)), it was assumed that the crystal structure of the resulting solid phase shows some similarities to the one of the starting material, especially in terms of the constitution of the layers. By comparing a simulated XRPD-pattern of $\alpha\text{-Li}_2\text{IrO}_3$ with the measured pattern $\text{H}_3\text{LiIr}_2\text{O}_6$, the latter seems to exhibit fewer diffraction lines (Fig. 3). A close inspection of the line profile, however, exhibits characteristic triangular, Warren-type³² peak shapes, *e.g.* at $(7\text{--}9)^\circ 2\theta$ and $(18.5\text{--}19.5)^\circ 2\theta$, which points to a pronounced stacking fault disorder. In consequence a number of reflections show broadening in such a way that they almost merge with the background, *e.g.* at 8.4 , 10.1 , 15.8 and $19^\circ 2\theta$. As the exact number and positions of all reflections, even at low diffraction angles was unknown, *ab initio* indexing by an iterative use of singular value decomposition³³ failed. Taking both the strong and the broadened weak reflections in the pattern of $\text{H}_3\text{LiIr}_2\text{O}_6$ into account (Fig. 3, blue line), similarities to the pattern of $\text{H}_3\text{LiIr}_2\text{O}_6$ can be recognized (Fig. 3, black line). For the determination of the space group symmetry and the lattice parameters it was assumed that the cation exchange did not cause fundamental structural change in $\alpha\text{-Li}_2\text{IrO}_3$, at least not in the $\text{LiIr}_2\text{O}_6^{3-}$ -layers. As almost all symmetry elements present in the crystal structure of $\alpha\text{-Li}_2\text{IrO}_3$ act within the layers, the $C2/m$ space group symmetry turned out to be a good

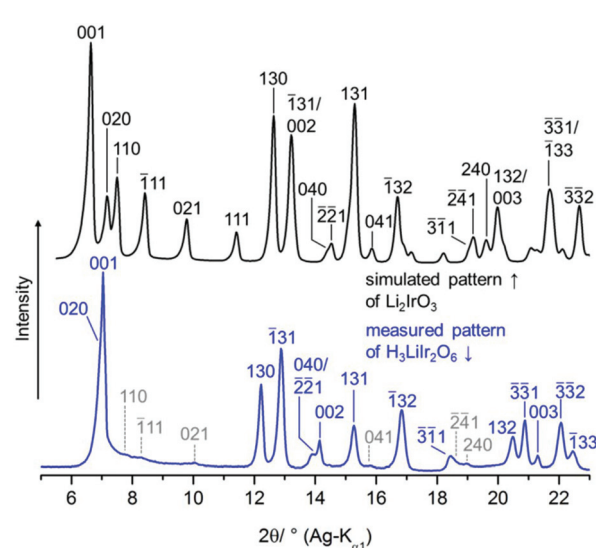


Fig. 3 Comparison of the measured XRPD-pattern of $\text{H}_3\text{LiIr}_2\text{O}_6$ including selected reflection indices assuming $C2/m$ space group symmetry, reflections that are vastly broadened due to faulting are indicated by grey font color and a simulated diffraction pattern of well-ordered Li_2IrO_3 , for the simulation the instrumental function of the diffractometer used for the XRPD measurement, was applied.



starting point for indexing the XRPD pattern of $\text{H}_3\text{LiIr}_2\text{O}_6$. Accordingly the intense basal reflection at $\approx 7^\circ 2\theta$ was indexed as 001. The upshift of this reflection from $\alpha\text{-Li}_2\text{IrO}_3$ to $\text{H}_3\text{LiIr}_2\text{O}_6$ (Fig. 3) indicates that the interlayer distance (product, $c\sin(\beta - 0.5\pi)$, of the lattice parameters c and β) of the latter phase is significantly smaller than in the starting material. In contrast some reflections like 130, $\bar{1}31$, 131 and $\bar{3}\bar{3}1$ show a downshift, which points to an elongation of the a - and/or b -axis after the cation exchange. The 020 reflection seems to be missing in the diffraction pattern of $\text{H}_3\text{LiIr}_2\text{O}_6$. A close inspection of the 001 reflection (Fig. 4), however, reveals an unusual peak shape. This reflection exhibits small shoulders both on the high and low angle side. The shoulder on the high angle side can be explained by an overlap with the Warren type peak, which, however, doesn't explain the shoulder on the low angle side.

This shoulder also can't be explained by the instrumental profile, as the 130 and $\bar{1}31$ reflections do not exhibit such a peak shape (Fig. 4). Accordingly the unusual profile of the 001 reflection must be caused by an overlap with another peak that is situated at a slightly lower diffraction angle. This was confirmed by a single line fit using two peaks. The additional reflection was indexed as 020 and its position pointed to a length of the b -axis of ≈ 9.24 Å. The information derived from the XRPD pattern was used for global optimization of the lattice parameters of $\text{H}_3\text{LiIr}_2\text{O}_6$ by a series of Pawley fits³⁴ employing the LP-search routine implemented into TOPAS.³⁵ The resulting global minimum was used as a starting model for the determination of precise lattice parameters by using a LeBail³⁶ fit and applying the fundamental parameter approach of TOPAS.²⁷

For the determination of the layer constitution of $\text{H}_3\text{LiIr}_2\text{O}_6$ the atomic positions of the $\text{LiIr}_2\text{O}_6^{3-}$ -layers of $\alpha\text{-Li}_2\text{IrO}_3$ were used as starting values. The inappropriate^{10,11} occupational disorder between Li and Ir on the metal site (2) in the structural model of O'Malley *et al.*⁹ was removed, as this is con-

sidered as an artefact of the refinement, caused by the occurrence of stacking faults. In order to avoid a correlation between the diffractional effects caused by the stacking faults and the refinement of the layer constitution, regions in the XRPD pattern that are affected by peak broadening ($7.18\text{--}11.88^\circ 2\theta$, $13.20\text{--}13.76^\circ 2\theta$, $14.30\text{--}15.00^\circ 2\theta$, $15.46\text{--}16.00^\circ 2\theta$, $17.24\text{--}20.25^\circ 2\theta$, $21.44\text{--}21.72^\circ 2\theta$ and $22.76\text{--}24.00^\circ 2\theta$) were excluded. Due to the exclusion of various regions of the XRPD pattern, an unconstrained refinement of the atomic coordinates and the lattice parameters was not possible, as the result strongly depends on the sequence in which the parameters were released to refinement. In addition, some resulting Ir-O and Li-O distances were either unreasonable long (>2.20 Å) or short (<1.80 Å). In order to introduce reasonable con- and restraints, the low distance region (<2.5 Å) of the measured PDF-curve was used, which refers to intralayer cation–oxygen distances (Fig. 5). The measured PDF-curve exhibits some noise and artefacts appearing as sine-type modulation in the region of low distances. Despite this noise a well-defined peak is clearly visible at 2.01 Å (Fig. 5, red font colour). This peak is mainly attributed to Ir–O pairs as more iridium than lithium is present in the solid and as iridium is a much stronger scatterer than lithium. According to the peak width and shape (small shoulder at higher distances) the distribution of the metal–oxygen distances is not necessarily unimodal and those distances can range from ≈ 1.90 Å to ≈ 2.10 Å. In consequence artificial penalty function depending on the metal–oxygen distances with minima at 2.0 Å both for the Ir–O and Li–O distances were included into the Rietveld refinements. This led to robust and reproducible results. During the refinement all atomic and lattice parameters were released iteratively and could be refined without using further con- or restraints. The crystallographic data and the refined atomic coordinates of $\text{H}_3\text{LiIr}_2\text{O}_6$ are given in Tables 1 and 2, the graphical result of the refinement and the agreement factors are presented in Fig. 6.

The obtained structural model of the $\text{LiIr}_2\text{O}_6^{3-}$ -layers of $\text{H}_3\text{LiIr}_2\text{O}_6$ can be evaluated as a reasonable approximation (see

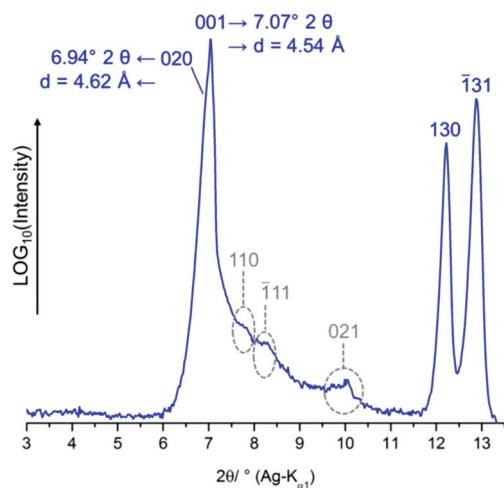


Fig. 4 Excerpts of the measured XRPD pattern of $\text{H}_3\text{LiIr}_2\text{O}_6$ including selected reflections indices.

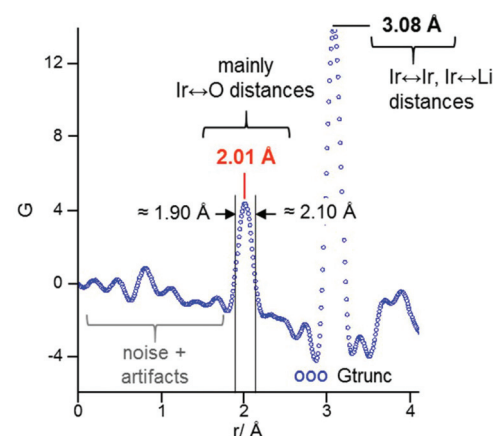


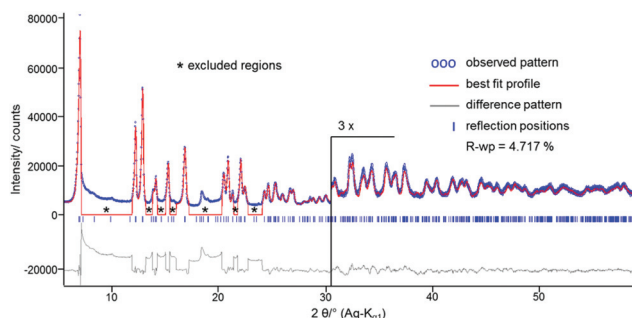
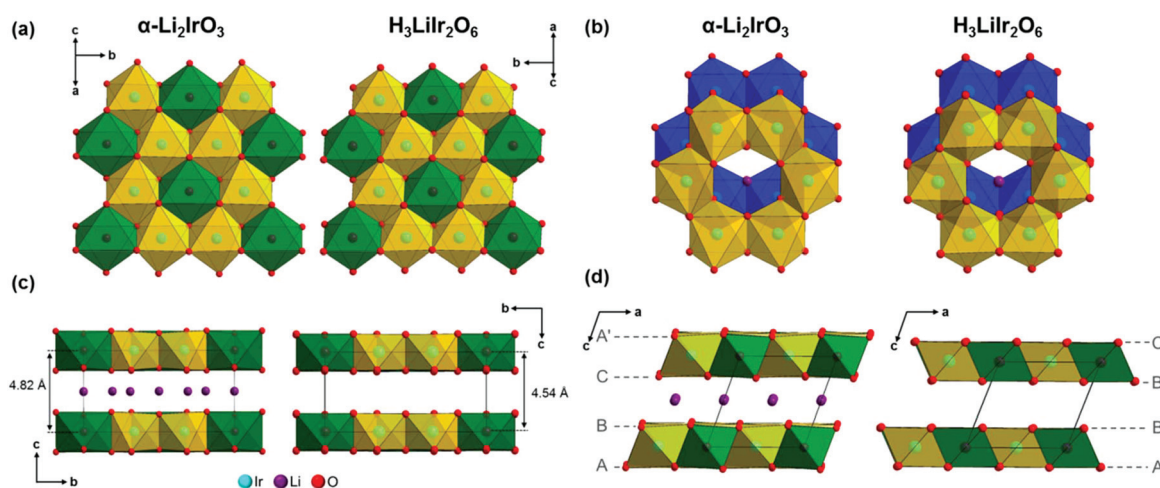
Fig. 5 Low r -region of the measured PDF-curve (blue circles) of synthesized $\text{H}_3\text{LiIr}_2\text{O}_6$. Contributions of Ir–O, Ir–Ir and Ir–Li pairs are highlighted.

Table 1 Space group symmetry and lattice parameters of α -Li₂IrO₃¹ and H₃LiIr₂O₆ (obtained by the LP-search routine)

	α -Li ₂ IrO ₃ ¹	H ₃ LiIr ₂ O ₆
Space group	<i>C</i> 2/ <i>m</i>	<i>C</i> 2/ <i>m</i>
<i>a</i> /Å	5.1633(2)	5.3489(8)
<i>b</i> /Å	8.9294(3)	9.2431(14)
<i>c</i> /Å	5.1219(2)	4.8734(6)
$\beta/^\circ$	109.759(3)	111.440(12)
<i>V</i> /Å ³	222.24(1)	224.27(6)

Table 2 Atomic coordinates of H₃LiIr₂O₆ at room temperature

Atom	Wyck.	Site	S.O.F.	<i>x</i>	<i>y</i>	<i>z</i>	<i>B</i> /Å ²
Ir1	4 <i>g</i>	2	1	0	0.335(3)	0	0.1(1)
Li1	2 <i>a</i>	2/ <i>m</i>	1	0	0	0	0.1(1)
O1	8 <i>j</i>	1	1	0.404(8)	0.323(3)	0.229(5)	1.7(3)
O2	4 <i>i</i>	<i>m</i>	1	0.417(8)	0	0.220(9)	1.7(3)

**Fig. 6** Scattered X-ray intensities of H₃LiIr₂O₆, at ambient conditions as a function of diffraction angle 2 θ . The observed pattern (circles) measured in Debye–Scherrer geometry, the best Rietveld fit profiles (line) using the LiIr₂O₆³⁻-layers of α -Li₂IrO₃ as starting model and the difference curve between the observed and the calculated profiles (below) are shown. The high angle part starting at 31.0° 2 θ is enlarged for clarity.**Fig. 7** Comparison of the LiIr₂O₆³⁻-layers in the crystal structures of α -Li₂IrO₃⁹ and H₃LiIr₂O₆. (a) plan view on the layers, (b) stacking of the Ir₆O₁₈¹²⁻ honeycombs (blue = bottom side layer, yellow = top side layer) with the IrO₆³⁻ octahedra omitted, (c) view in *a*-, (d) view in *b*-direction.

below). According to the limits of the XRPD method no attempt was made to determine and refine the hydrogen positions. The stacking pattern of the LiIr₂O₆³⁻-layers of H₃LiIr₂O₆ in the structural model is determined by the lattice parameters and the space group symmetry. According to the pronounced occurrence of stacking faults, the obtained structural model cannot be considered as the crystal structure of H₃LiIr₂O₆, but it will serve as a starting point for a detailed investigation of the microstructure of H₃LiIr₂O₆.

Crystal structure description of H₃LiIr₂O₆ in relation to α -Li₂IrO₃

A comparison of the crystal structure of the starting material and the product after the cation exchange by acid treatment is presented in Table 1 and Fig. 7. For this comparison it was assumed that α -Li₂IrO₃ does not exhibit any occupational disorder between Li and Ir in the LiIr₂O₆³⁻-layers. The layers of H₃LiIr₂O₆ consist of edge linked, distorted LiO₆- and IrO₆-octahedra that form sheets within the *ab*-plane of the unit cell (Fig. 7a, on the right). Within these layers each LiO₆³⁻-octahedron (Fig. 7, green) is surrounded by six IrO₆³⁻-octahedra (yellow) and each oxygen atom is coordinated by two iridium ions and one lithium ion. Hence, the cation exchange did not produce significant changes in the cation sublattice (Fig. 7a). Due to the exchange of Li⁺ by less space filling H⁺, the interlayer distance was shortened from 4.82 Å in α -Li₂IrO₃ to 4.54 Å in H₃LiIr₂O₆ (Fig. 7c) and the arrangement of the layers, *i.e.* the stacking order, was altered. The LiIr₂O₆³⁻-layers in α -Li₂IrO₃ are stacked in a monoclinic distorted CdCl₂ (C19-type) like fashion with an ABCA'B'C'A''B''C''... stacking pattern of the anions, whereas the layers in H₃LiIr₂O₆ are stacked in a monoclinic distorted HCrO₂ (3R-type) like way with an ABBCCA'A'B'B'C'C''... stacking pattern of the anions (Fig. 7b and d). In addition, slight changes in the anion sublattice are obvious. By the partial protonation of oxide ions during the cation exchange, hydroxide ions are formed. As the stacking



order of $\text{H}_3\text{LiIr}_2\text{O}_6$ indicated that anions of neighboring layers directly oppose each other, attractive $\text{O}\cdots\text{H}\cdots\text{O}$ interactions, most likely hydrogen bonds, between anion sites of neighboring layers can be assumed. In consequence, the curly character of the sheets, *i.e.* the distance between the planes in which the two oxygen sites are situated, is much less pronounced in $\text{H}_3\text{LiIr}_2\text{O}_6$ than in $\alpha\text{-Li}_2\text{IrO}_3$ (Fig. 7c and d).

A comparison of the distorted $\text{LiO}_{6/3}^{3-}$ - and $\text{IrO}_{6/3}$ -octahedra in $\alpha\text{-Li}_2\text{IrO}_3$ and $\text{H}_3\text{LiIr}_2\text{O}_6$ is given in Fig. 8 and the metal–oxygen distances are listed in Table 3. In general the coordination polyhedra are only little affected by the cation exchange, only some bond distances in the LiO_6 -octahedra in $\text{H}_3\text{LiIr}_2\text{O}_6$ are slightly elongated compared to $\alpha\text{-Li}_2\text{IrO}_3$, whereas the IrO_6 -octahedra exhibits almost no change. All metal–oxygen distances are in reasonable range. The distances between the cations (Table 3, bottom) are slightly elongated. The obtained values (3.06 Å–3.10 Å), however, are in very good agreement with the PDF-data (Fig. 5). As no penalty function was applied on the distances between the cations, these results indicate that a suitable model of the layer constitution was derived by Rietveld refinement.

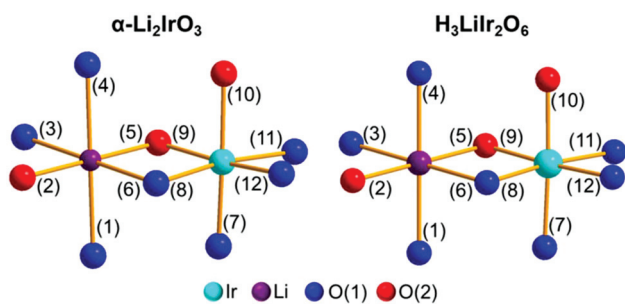


Fig. 8 $\text{LiO}_{6/3}^{3-}$ and $\text{IrO}_{6/3}$ polyhedra in the crystal structures of $\alpha\text{-Li}_2\text{IrO}_3$ ⁹ and $\text{H}_3\text{LiIr}_2\text{O}_6$, the distances between metal- and oxygen sites are labeled and listed in Table 3.

Table 3 Comparison of the metal–oxygen and metal–metal distances in the crystal structures of $\alpha\text{-Li}_2\text{IrO}_3$ ⁹ and $\text{H}_3\text{LiIr}_2\text{O}_6$

Distance no. (Fig. 8)	Distance between atoms	Distance/Å	
		$\alpha\text{-Li}_2\text{IrO}_3$	$\text{H}_3\text{LiIr}_2\text{O}_6$
(1)	Li–O(1)	2.19(1)	2.15(3)
(2)	Li–O(2)	1.97(2)	2.08(6)
(3)	Li–O(1)	2.19(1)	2.15(3)
(4)	Li–O(1)	2.19(1)	2.15(3)
(5)	Li–O(2)	1.97(2)	2.08(6)
(6)	Li–O(1)	2.19(1)	2.15(3)
(7)	Ir–O(1)	1.97(1)	2.01(3)
(8)	Ir–O(1)	2.08(2)	2.04(3)
(9)	Ir–O(2)	2.01(1)	2.01(3)
(10)	Ir–O(2)	2.01(1)	2.01(3)
(11)	Ir–O(1)	2.08(2)	2.04(3)
(12)	Ir–O(1)	1.97(1)	2.01(3)
—	Ir–Ir	$3 \times 2.98(1)$	$2 \times 3.10(1)$ $1 \times 3.06(1)$
—	Ir–Li	$4 \times 2.98(1)$	$2 \times 3.09(1)$ $2 \times 3.08(1)$

The cation sublattice of $\text{H}_3\text{LiIr}_2\text{O}_6$ reveals a pronounced pseudo symmetry. A pseudo trigonal lattice as described by O’Malley *et al.*¹ can be found with a ≈ 3.1 Å (ESI, Fig. S2,† grey lines), which symmetry is broken by the ordering between Li and Ir. In addition the $\text{Ir}_6\text{O}_{18}^{12-}$ honeycombs (Fig. 7b, blue octahedra) exhibit a very pronounced pseudo hexagonal symmetry (ESI, Fig. S2,† green lines) that is only broken by the stacking order of the layers (see next sections).

Derivation of the stacking pattern and of potential structural defects. Recently the real structures of related stacking faulted iridates with honeycomb like lattices were successfully described by super positioning of different stacking types.^{10,11} Based on these approaches possible stacking orders of the layers are derived from structural considerations.

The arrangement of the layers, *i.e.* the stacking order, in $\text{H}_3\text{LiIr}_2\text{O}_6$ can be described by a stacking vector **S1** that is identical with the *c*-axis of the monoclinic unit cell. The stacking pattern of the layers results almost in a CrOOH like stacking, $(\text{AyB})(\text{BoC})(\text{C}\beta\text{A})(\text{AyB})^i(\text{BoC})^i(\text{C}\beta\text{A})^i(\text{AyB})^{i+1}(\text{BoC})^{i+1} \dots$, with anion positions indicated by capital Latin letters, anion positions indicated by small Greek letters and layers indicated by parenthesis (Fig. 9a). The stacking order exhibits a monoclinic distortion, *i.e.* layer $i + 3$ is not identical with layer i , which is indicated by superscripted *I* and *I* + 1. Anions of neighboring layers are situated almost in direct opposition to each other. According to the limits of the XRPD-method no attempt was made to determine and refine the hydrogen positions of the crystal structure. Due to the low interlayer spacing and the short O–O distances (Fig. 9a) strong attractive interaction between the sheets, most likely mediated by hydrogen bonds can be expected. Hence the hydrogen atoms should be located at positions forming an O(layer i)-H–O(layer $i + 1$) angle of approx. 180° . With a stacking of the layers in a **S1**-pattern all oxygen sites of adjacent layers directly oppose each other. This leads to strong $\text{O}(2)\cdots\text{H}\cdots\text{O}(2)$ contacts with $d(\text{O}(2)\cdots\text{H}\cdots\text{O}(2)) =$

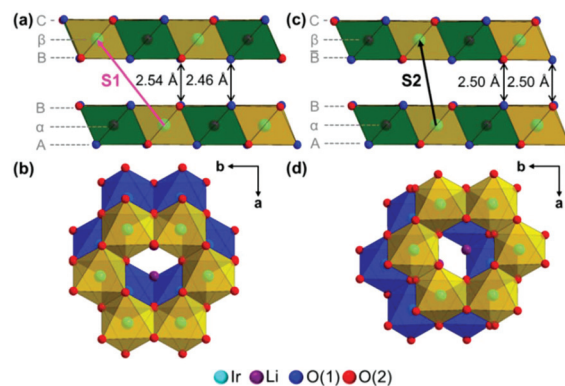


Fig. 9 Possible stacking patterns of $\text{H}_3\text{LiIr}_2\text{O}_6$ (a) stacking in the structure model obtained by Rietveld refinement with stacking vector **S1** describing the stacking sequence of the layer, (b) **S1**-stacking of the $\text{Ir}_6\text{O}_{18}^{12-}$ honeycombs (blue = bottom side layer, yellow = top side layer) with the $\text{LiO}_{6/3}^{3-}$ octahedra omitted (c) alternative stacking pattern of $\text{H}_3\text{LiIr}_2\text{O}_6$ with stacking vector **S2**, (d) **S2**-stacking of the $\text{Ir}_6\text{O}_{18}^{12-}$ honeycombs with the $\text{LiO}_{6/3}^{3-}$ octahedra omitted.

2.54 Å and O(1)…H–O(1) contacts with $d(\text{O1–O1}) = 2.46$ Å (Fig. 9a). With respect to the site multiplicity (O(1) = 8*j* site and O(2) = 4*i* site) pure S1-stacking provides 2 very strong and 4 strong hydrogen bonds.

In the crystal structure of $\text{H}_3\text{LiIr}_2\text{O}_6$ the arrangement of the layers can be altered by using a different stacking vector, S2, in such a way that 8 out of 12 oxygen sites directly oppose each other (Fig. 9c) by forming O(2)…H–O(1) and O(1)…H–O(2) contacts. Hence the anions of layer *i* are directly opposed by anions of layer *i* + 1, as well, but O(1) is now in opposition of O(2), which is indicated by a bar on top of the anion layer label. The resulting $(\text{AyB})(\bar{\text{B}}\alpha\text{C})(\bar{\text{C}}\beta\text{A})(\bar{\text{A}}\gamma\text{B})^i(\bar{\text{B}}\alpha\text{C})^j(\bar{\text{C}}\beta\text{A})^i(\bar{\text{A}}\gamma\text{B})^{i+1}(\bar{\text{B}}\alpha\text{C})^{i+1}\dots$ stacking pattern provides 4 strong O(2)…H–O(1) and O(1)…H–O(2) contacts with $d(\text{O1–O2}) = 2.50$ Å and 4 oxygen sites (half of the O(2) sites) are located almost in direct opposition to each other (Fig. 10b). Hence hydrogen bonds between these sites can only be formed if the bond between oxygen and hydrogen in a hydroxide ion is canted. This S2-stacking pattern with 4 strong hydrogen bonds and 2 bonds with potentially canted hydroxide ions should be energetically a little less favored with respect to the S1-stacking pattern with 6 strong and hydrogen bonds (Fig. 10a). Nevertheless, within the S1-stacking pattern of $\text{LiIr}_2\text{O}_3(\text{OH})_3$ layers stacked in an alternative, S2-like way, can appear as stacking faults.

Alternative stacking vectors can be derived directly from the constitution of the layers. Due to the sharp 00*l* reflection in the diffraction pattern of $\text{H}_3\text{LiIr}_2\text{O}_6$ (Fig. 12, blue line) the interlayer spacing is not affected by stacking faults, *i.e.* the *z*-component of each stacking vector must be 1.0. The stacking vector S1 (Fig. 11a, magenta) directs an oxygen site, *e.g.* O2, in direct opposition to an identical site (red ball) of the preceding layer. Alternative stacking vectors bring different oxygen atoms in the surrounding of this O2-site in direct opposition to the O2 site of the preceding layer. Thus the *x*- and *y*-components of alternative stacking vectors can be derived from a projection of an oxygen layer onto the *ab*-plane (Fig. 11b). Therefore, the position of one O2 site is used as the origin for fractional *x*- and *y*-coordinates using *a*- and *b*-lattice parameters. There are four O2 sites in direct surrounding of an O2 site, each of these positions can be reached by a shift, denoted as S1-1, of $x = \pm 1/2$

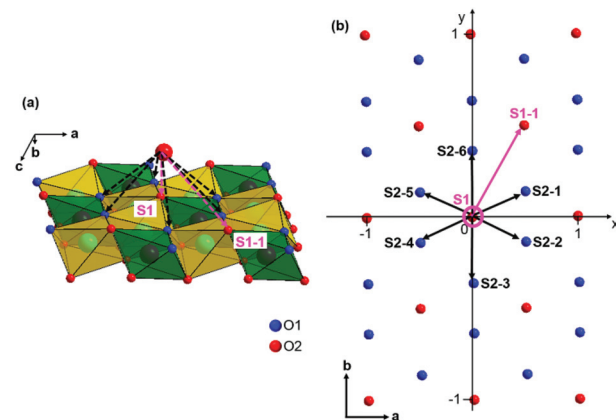


Fig. 11 Derivation of potential stacking vectors in the microstructure of $\text{H}_3\text{LiIr}_2\text{O}_6$ by considering all potential O–H–O contacts of adjacent layers (a), projection of the oxygen sites at the bottom site of subsequent layer onto the *ab*-plane (b).

and $y = \pm 1/2$. Due to layer symmetry, with symmetry centers at $(0,0)$; $(\pm 1/4, \pm 1/4)$ and $(\pm 1/2, \pm 1/2)$, each of these shifts is symmetry equivalent to S1 and therefore transitions among S1 and S1-1 stacking won't produce any additional diffraction effects. Six O1 sites are located in direct surrounding of one O2 site, as well. The shift from O2 to any of these sites produces a S2 like stacking described above. Accordingly, six alternative stacking vectors (S2-1 to S2-6) can be derived from the relative positions of O1 sites surrounding a central O2 site (Table 4).

In a hexagonal lattice all stacking vectors would be equal. The symmetry is broken, as one stacking vector, S1, seems to be preferred.

Systematic DIFFaX-studies

The DIFFaX-routine³⁷ was used to simulated the diffraction patterns of stacking faulted $\text{LiIr}_2\text{O}_3(\text{OH})_3$, containing transitions among S1 and S2-*i*-stacking. The simulations were carried out in recursive mode, *i.e.* an average diffraction pattern of all possible stacking sequences, weighted by transition probabilities is calculated in each simulation. The number of layers and the

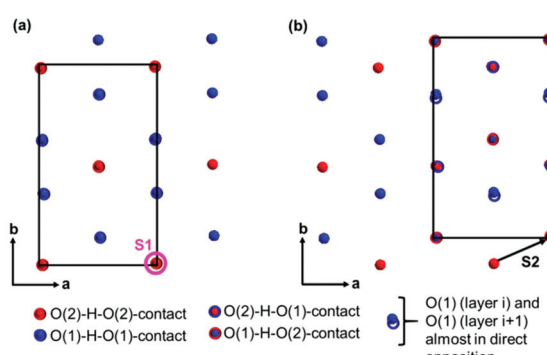


Fig. 10 Effect of (a) S1 and (b) S2 stacking on O–H–O interlayer-contacts of adjacent layers.

Table 4 Overview on potential stacking vectors in the microstructure of $\text{H}_3\text{LiIr}_2\text{O}_6$ derived by considering all potential O–H–O contacts of adjacent layers

Stacking vector	Stacking vector components			
	S_x	S_y	S_z	
S1	0	0	1	O(1)…H–O(1)
S1-1	$\pm 1/2$	$\pm 1/2$	1	O(2)…H–O(2)
S2-1	0.4890	0.1770	1	O(1)…H–O(2)
S2-2	0.4890	-0.1770	1	O(2)…H–O(1)
S2-3	-0.0110	-0.3230	1	
S2-4	-0.5110	-0.1770	1	
S2-5	-0.5110	0.1770	1	
S2-6	-0.0110	0.3230	1	



layer extension in *a*- and *b*-direction was set to infinite. A Pseudo-Voigt function, derived from a LeBail-fit³⁶ of the measured diffraction pattern without using crystalline size parameters, was used to describe the peak profile.

Transformation of the unit cell and the atomic coordinates.

As only unit cells with $\alpha, \beta = 90^\circ$ and $\gamma = \text{variable}$ can be used in the DIFFaX-routine, a transformation of the monoclinic unit cell of $\text{H}_3\text{LiIr}_2\text{O}_6$ into an orthorhombic one with $\alpha, \beta, \gamma = 90^\circ$, was necessary. Therefore, a new, β -dependent, *c*'-axis had to be defined (Table 5). In addition all atomic coordinates (*x*, *y*, *z*), as well as the *x*-, *y*- and *z*-components of the stacking vectors (Table 4) were adopted to the transformed *c*' and β' lattice parameters using (eqn (1)). Due to the translational symmetry, the simulations can be limited to 4 stacking vectors: **S1**, **S2-1**, **S2-2** and **S2-3**. A 4×4 matrix of transition probabilities, P_{ij} , (Table 6) was used to describe different degrees of faulting in the crystal structure of $\text{H}_3\text{LiIr}_2\text{O}_6$.

$$\begin{pmatrix} x' \\ y' \\ z' \end{pmatrix} = \begin{pmatrix} \left(x - \frac{z \cdot c \cdot \sin(\beta - \frac{\pi}{2})}{a} \right) \\ y \\ z \end{pmatrix} \quad (1)$$

Diffraction effects of stacking faults within the structure of $\text{LiIr}_2\text{O}_3(\text{OH})_3$. As a starting point the diffraction pattern of faultless $\text{H}_3\text{LiIr}_2\text{O}_6$ using pure **S1**-stacking with $P_{11} = 1.0$ was simulated (Fig. 12, black line) and compared to the measured pattern (blue line) of the sample. In the measured diffraction

Table 5 Transformation of the unit cell of $\text{H}_3\text{LiIr}_2\text{O}_6$ into a DIFFaX-compatible setting

Original unit cell	Transformed unit cell
<i>a</i> 5.3489 Å	<i>a'</i> = <i>a</i> 5.3489 Å
<i>b</i> 9.2431 Å	<i>b'</i> = <i>b</i> 9.2431 Å
<i>c</i> 4.8734 Å	<i>c'</i> = <i>c</i> · cos($\beta - 0.5 \cdot \pi$) 4.5362 Å
α 90°	α' = α 90°
β 111.440°	β' 90°
γ 90°	γ' = γ 90°

Table 6 Stacking vectors and transition probability matrix used for the DIFFaX-simulations

Stacking vector	Stacking vector components		
	S_x	S_y	S_z
S1	-0.3330	0	1
S2-1	0.1560	0.1770	1
S2-2	0.1560	-0.1770	1
S2-3	-0.3440	-0.3230	1

Transition probabilities

From ↓	To →	S1	S2-1	S2-2	S2-3
S1		P_{11}	P_{12}	P_{13}	P_{14}
S2-1		P_{21}	P_{22}	P_{23}	P_{24}
S2-2		P_{31}	P_{32}	P_{33}	P_{34}
S2-3		P_{41}	P_{42}	P_{43}	P_{44}

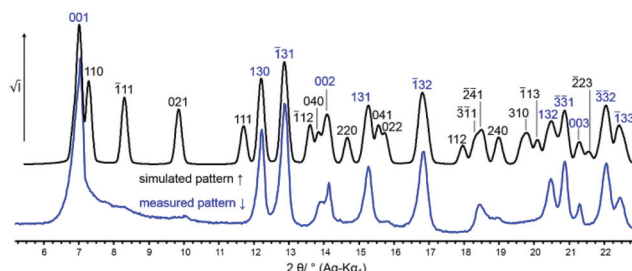


Fig. 12 Measured (blue) and simulated (black) XRPD-pattern of a faultless sample of $\text{H}_3\text{LiIr}_2\text{O}_6$ with pure **S1**-stacking.

pattern only sharp $00l$, $13l$, $\bar{1}3l$ and $\bar{3}\bar{3}l$ reflections are apparent (Fig. 12, blue indices). All other reflections are broadened in such a way that they almost completely merge with the background. Broadening of the 110 , $\bar{1}11$, 021 , $\bar{2}\bar{4}1$ and 240 reflections leads to a characteristic triangular peak shape³² that indicates heavy faulting by random transitions among several stacking vectors. In addition, no further, sharp reflections are present in the measured diffraction pattern, hence the existence of domains of homogenous, **S2-i** stacked sections in the microstructure of $\text{H}_3\text{LiIr}_2\text{O}_6$ can be excluded. There are some tiny remnants of the $\bar{1}11$, 021 , 041 , 022 and 240 reflections in the measured diffraction pattern, which indicate that despite heavy faulting **S1**-stacking is still present in the microstructure and that small **S1**-stacked sections are apparent.

The observed peak broadening and triangular peak shape in combination with structural considerations (Fig. 11) were used to introduce constraints for the transition probabilities, P_{ij} , to simplify the 4×4 transition probability matrix for systematic DIFFaX-simulations. As each alternative stacking vector, **S2-i** leads to the same number of strong O-H-O contacts, there shouldn't be any preference for any of these vectors after a shift from **S1** stacking. Accordingly, the probability for a shift from **S1**-type stacking to **S2**-type stacking must be equal for all **S2-i** stacking vectors. In consequence the probability of a fault in an **S1** stacking pattern can be described with the parameter *x* (Table 7). As each line of the transition probability matrix has to sum up to 1.0, each transition probability from **S1** to **S2-i** can be expressed as *x*/3. With respect to the constitution of the layers, a shift from **S1**-stacking to **S2-i** does not implement any preference for a continuation of the **S2-i** stacking pattern, *i.e.* stacking faults do not have any range. This is indicated by the absence of additional, sharp reflections in the measured diffraction pattern of $\text{H}_3\text{LiIr}_2\text{O}_6$. Hence each line of the transition probability matrix

Table 7 Constrained transition probability matrix, used for a systematic DIFFaX-study, with increasing probability, *x*, of a fault within **S1**-stacking

From ↓	To →	S1	S2-1	S2-2	S2-3
S1		1 - <i>x</i>	<i>x</i> /3	<i>x</i> /3	<i>x</i> /3
S2-1		1 - <i>x</i>	<i>x</i> /3	<i>x</i> /3	<i>x</i> /3
S2-2		1 - <i>x</i>	<i>x</i> /3	<i>x</i> /3	<i>x</i> /3
S2-3		1 - <i>x</i>	<i>x</i> /3	<i>x</i> /3	<i>x</i> /3



can be expressed by the same set of transitions probabilities (Table 7). In consequence a systematic DIFFaX study could be carried out by varying only one parameter, x , describing the probability of faulting in the **S1**-stacking pattern of $\text{H}_3\text{LiIr}_2\text{O}_6$.

The results of the systematic DIFFaX-study are summarized in Fig. 13. As predicted, increasing faulting in the **S1**-stacking of the crystal structure of $\text{LiIr}_2\text{O}_3(\text{OH})_3$ leads to broadening of all non $00l$, $13l$, $\bar{1}3l$ and $\bar{3}3l$ reflections. The higher the degree of faulting, x , the greater the similarity between simulated and measured diffraction patterns. In addition, triangular peaks shapes evolve by broadening of the 110 , $\bar{1}11$, 021 , $\bar{2}41$ and 240 reflections. At $x = 0.4$ the greatest similarity between simulated (Fig. 13, dark magenta line) and measured (blue line) XRPD pattern is reached. A further increase of the degree of faulting, which is identical with a complete random stacking using **S1** and **S2-i** vectors, will lead to disappearance of the remnants of the 111 , 021 , 041 and 240 reflections. As only a finite number of crystals, having a limited crystalline size and therefore a limited number of layer-to-layer-transitions, contributed to the

measured diffraction pattern and as recursive DIFFaX-simulations led to diffraction patterns, produced by an infinite number of crystals, there can't be a complete match between simulated and measured patterns. In addition in the DIFFaX-simulation only idealized stacking vectors were used, that were created on the assumption, that the O-H bond is orientated perpendicular to the layers, which is not necessarily the case, taking the asymmetric coordination spheres of the oxygen sites ($2x$ Ir, $1x$ Li) into account. Nevertheless, a good agreement was reached, which confirms that a realistic microstructural model has been developed. The degree of faulting in the **S1**-stacking pattern, $x = 0.4$, that created the best agreement between the simulated and measured pattern, however, is most likely slightly different in the real microstructure of the sample. Hence a Rietveld compatible approach was used, that allowed the refinement of the stacking vectors.

Rietveld compatible approach

In order to confirm the microstructural model derived from structural considerations and DIFFaX-simulations the Rietveld compatible approach^{38–40} was used for global optimization of a limited supercell representing the microstructure of the sample. In this approach each layer is treated as a rigid body. During global optimization the layers are allowed to move unconstrained and unrestrained in their *ab*-plane. A 12 *c* supercell containing 12 layers was subjected to global optimization using the simulated annealing approach⁴¹ implemented into TOPAS. The resulting stacking vectors were calculated from each layer position in relation to the preceding layer with the first layer of the unit preceded by the last one.

Although the movement of the layer was not restrained each stacking vector within the supercell refined very close ($\approx \pm 0.03x$, $\pm 0.02y$) to an idealized pendant derived from structural considerations (Table 8). This means that the free unconstrained movement of the layers led to a stacking

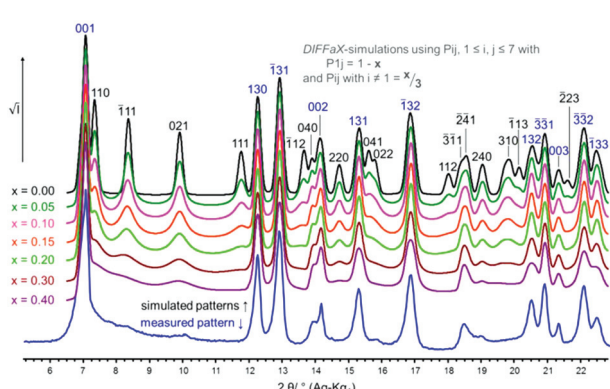


Fig. 13 Measured XRPD-pattern (blue) and simulated patterns of stacking faulted of $\text{H}_3\text{LiIr}_2\text{O}_6$.

Table 8 Comparison of stacking vectors obtained by global optimization of a 12 *c* supercell of $\text{H}_3\text{LiIr}_2\text{O}_6$ using uncon- and unrestrained movement of 12 rigid body like layers in *x*- and *y*-direction with their idealized pendants derived from structural considerations

Global optimization of the XRPD-pattern			Idealized structure model (Table 4)			Deviation	
Transition From layer <i>i</i> to layer <i>i</i> + 1	Stacking vector		Stacking vector			Optimized ↔ idealized	
	<i>x</i> -Component	<i>y</i> -Component	<i>x</i> -Component	<i>y</i> -Component	Assignment	<i>x</i> -Component	<i>y</i> -Component
1 → 2	0.5043	-0.1693	0.4890	-0.1770	≡ S2-2	0.0153	0.0077
2 → 3	0.5165	0.1805	0.4890	0.1770	≡ S2-1	0.0275	0.0035
3 → 4	0.0090	-0.0001	0	0	≡ S1	0.0090	-0.0001
4 → 5	0.0080	0.0006	0	0	≡ S1	0.0080	0.0006
5 → 6	0.0031	0.0039	0	0	≡ S1	0.0031	0.0039
6 → 7	0.0079	-0.3240	-0.0110	-0.3230	≡ S2-3	0.0189	-0.0010
7 → 8	-0.0020	-0.3308	-0.0110	-0.3230	≡ S2-3	0.0090	-0.0078
8 → 9	0.5038	0.1710	0.4890	0.1770	≡ S2-1	0.0148	-0.0060
9 → 10	0.0119	-0.3288	-0.0110	-0.3230	≡ S2-3	0.0229	-0.0058
10 → 11	0.4885	0.4839	1/2	1/2	≡ S1-1	-0.0115	-0.0161
10 → 12	0.4837	0.4878	1/2	1/2	≡ S1-1	-0.0163	-0.0122
12 → 1 ^a	0.5053	-0.1747	0.4890	-0.1770	≡ S2-2	0.0163	0.0023

^a Due to translation symmetry, layer 12 is followed by layer 1 of the subsequent unit cell.

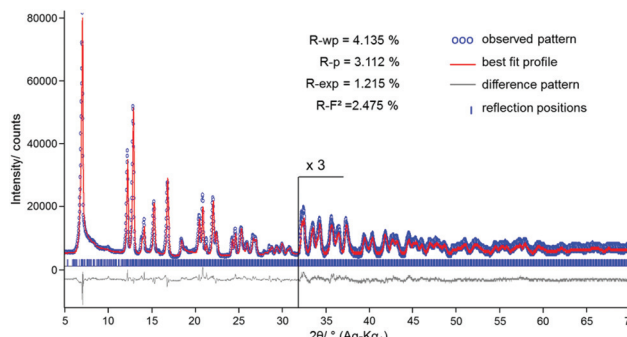


Fig. 14 Scattered X-ray intensities of $\text{H}_3\text{LiIr}_2\text{O}_6$, at ambient conditions as a function of diffraction angle 2θ . The observed pattern (circles) measured in Debye–Scherrer geometry, the best Rietveld fit profiles (line) using a 12 c supercell and the difference curve between the observed and the calculated profiles (below) are shown. The high angle part starting at $21.0^\circ 2\theta$ is enlarged for clarity.

pattern in which all oxygens of neighbouring layers are almost on direct opposition to each other. **S1**-like stacking is dominant and small **S1**-stacked sections are present, which breaks the hexagonal symmetry, whereas transitions to and among **S2**-like stacking occur unsystematically. The obtained supercell provides good agreement between calculated and measured diffraction pattern with good agreement factors (Fig. 14).

PDF-analysis

In order to support the microstructure model of $\text{H}_3\text{LiIr}_2\text{O}_6$ obtained by a Rietveld compatible approach using low energy (22.16 keV \equiv 0.5594 Å) laboratory X-ray diffraction data PDF-analyses were performed using high energy (67.13 keV \equiv 0.1847 Å) synchrotron XRPD data collected at the X28 beamline of NSLS-II (Brookhaven Nat. Lab.). PDF-curves were calculated (Fig. 15, red line) from the HCrO_2 like crystal structure model of O'Malley *et al.*¹ (a), from a faultless monoclinic structure model with pure **S1**-stacking (b) obtained by a constraint Rietveld refinement (Fig. 6, Tables 1 and 2) and from the 12 c (12 layer) supercell structure (Fig. 15c) by a Rietveld compatible global optimization using rigid body like layers (Table 8, Fig. 14) and compared to the measured curve (Fig. 15, blue circles). Atomic and lattice parameters were kept fixed for all calculations.

PDF-analysis clearly demonstrates that the HCrO_2 like structure model of O'Malley *et al.*¹ is not suitable as the match between measured and calculated curve is poor both in low and high distance region (Fig. 15a). The exact position of the first peak at ≈ 2.0 Å, referring mainly to Ir–O pairs cannot be described by this structure model, which means the constitution of the layers differs from the expected HCrO_2 like structure model. In addition the misfit at higher distances indicates a different stacking pattern, as well. In contrast for the monoclinic structure model with pure **S1**-stacking there is a good match between calculated and measured curve at low distances ($r < 7.0$ Å) indicating that the constitution of the layers was

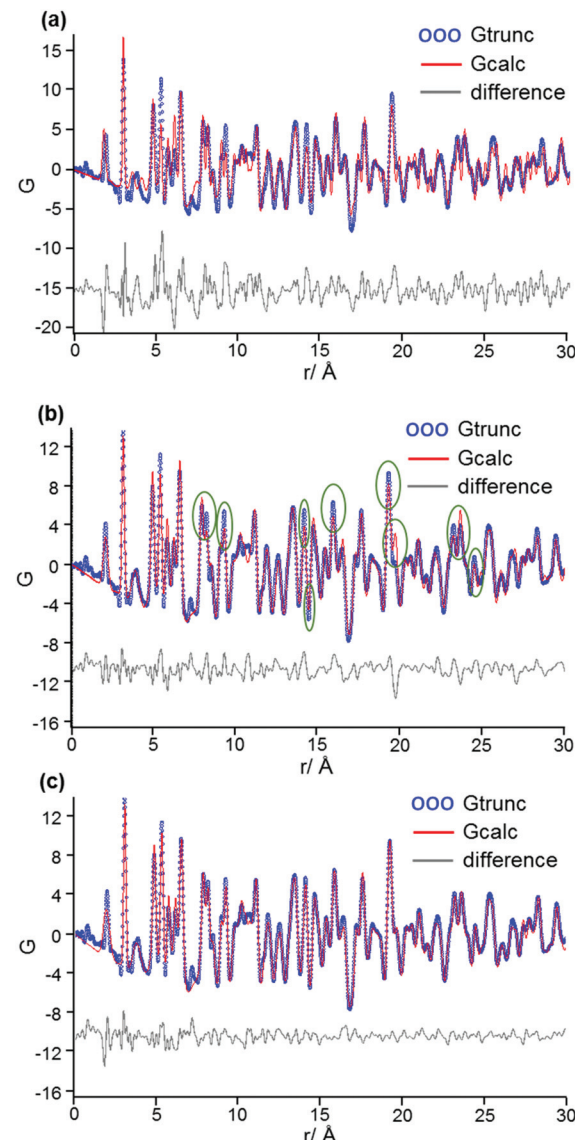


Fig. 15 PDF-curve (blue), calculated curve (red) and difference curve (grey) of $\text{H}_3\text{LiIr}_2\text{O}_6$, (a) using the HCrO_2 like structure model of O'Malley *et al.*¹ (b) using a faultless monoclinic structure model with pure **S1** stacking, serious misfits are indicated by green ellipses (c) using a 12 c (12 layers) supercell obtained by global optimization (Table 8, Fig. 14).

refined properly (Fig. 15b). At high distances referring to interlayer pairs, however, there are serious deviations of the calculated PDF-curve from the measured one (green ellipses), which can be attributed to the occurrence of stacking faults.⁴⁰ The usage of the structural data of the faulted 12 c supercell leads to a substantial improvement of the fit especially in the region of high interatomic distances ($r > 7.0$ Å). The match in this region is almost perfect. Thus the microstructure model which was obtained by structural considerations (Fig. 11, Table 4), DIFFaX-simulations (Table 6, Fig. 13) and Rietveld compatible global optimization using rigid body like layers (Table 8, Fig. 14) describes essential features of disorder in the crystal structure of $\text{H}_3\text{LiIr}_2\text{O}_6$.



Conclusions

A sample of pure $H_3LiIr_2O_6$ was synthesized by using α - Li_2IrO_3 as a starting material and replacing Li^+ by H^+ employing soft chemical methods. The honeycomb crystal structure of $H_3LiIr_2O_6$ was investigated by high resolution laboratory and synchrotron X-ray powder diffraction. Strong anisotropic broadening of the reflections in the XRPD-pattern revealed heavy stacking faulting of the sample. An idealized structural model, with sheets of edge sharing LiO_6 - and IrO_6 -octahedra forming a honeycomb structure, could be derived from the low energy laboratory powder diffraction data using constraints derived from PDF analysis of the high energy synchrotron powder diffraction data, as well as solid state NMR spectroscopy as a complementary tool. The LiO_6 - IrO_6 -octahedra-layers are interconnected by strong $O-H\cdots O$ contacts. Different possible stacking patterns that bring oxygen sites of adjacent layers in direct opposition and therefore provide the strongest $O-H\cdots O$ contacts were derived from the layer constitution. Hence a slight preference of the stacking pattern, **S1**, which brings all oxygen atoms in direct opposition, towards six alternative sequences, **S2-1** to **S2-6**, which brings only 2/3 of the oxygen atoms of adjacent layers in direct opposition can be expected. On this basis a microstructural model of $H_3LiIr_2O_6$ with **S1**-basic stacking that is randomly interrupted by **S2-*i***-stacked sheets could be developed and confirmed by DIFFaX-simulations as well as by global optimization of a supercell containing 12 layers. PDF analysis, in particular the higher radial distances was also successfully employed as complementary tool to confirm the obtained microstructure model. Due to the unconstrained and restrained layer movement during the Rietveld compatible global optimization, as well as due to the limited extension of the supercell this approach can be considered as an approximation to the real microstructure. The usage of a more extended supercell would lead to a further overextension of the parameter space. Nevertheless, a good match between measured and calculated pattern could be reached, with stacking vectors close to the expected values. The obtained stacking sequence is in good qualitative agreement to the microstructural model derived from structural considerations and DIFFaX-simulations and additionally confirmed by the PDF analysis. Hence the microstructural model presented in this study is confirmed.

The approach for the determination of the faultless, ideal crystal structure and the kind and amount of faulting, *i.e.* the real crystal structure, presented in this can be adapted to all other, related layered honeycomb materials of interest, *e.g.* $Cu_3LiIr_2O_6$,⁴² $Cu_3NaIr_2O_6$ ⁴² and $Ag_3LiIr_2O_6$.⁴³

Conflicts of interest

There are no conflicts to declare.

Acknowledgements

Mrs Christine Stefani from Max-Planck-Institute for Solid State research is acknowledged for performing the laboratory XRPD

measurements. Dr Melinda Abeykoon and Dr Eric Dooryhee from Brookhaven National Laboratory are acknowledged for their support at the X28 beamline. Maxwell Terban from the Columbia University is acknowledged for taking the synchrotron XRPD patterns.

Funding by DFG for the project "In search of structure" (grant EG 137/9-1) and Open Access funding provided by the Max Planck Society is gratefully acknowledged.

References

- 1 M. J. O'Malley, P. M. Woodward and H. Verweij, *J. Mater. Chem.*, 2012, **22**, 7782.
- 2 I. Lauks, M. F. Yuen and T. Dietz, *Sens. Actuators*, 1983, **4**, 375–379.
- 3 A. Fog and R. P. Buck, *Sens. Actuators*, 1984, **5**, 137–146.
- 4 S. Glab, A. Hulanicki, G. Edwall and F. Ingman, *Crit. Rev. Anal. Chem.*, 1989, **21**, 29–47.
- 5 S. Yao, M. Wang and M. Madou, *J. Electrochem. Soc.*, 2001, **148**, H29.
- 6 M. Wang, S. Yao and M. Madou, *Sens. Actuators, B*, 2002, **81**, 313–315.
- 7 M. Wang and S. Yao, *Electroanalysis*, 2003, **15**, 1606–1615.
- 8 H. Kobayashi, M. Tabuchi, M. Shikano, H. Kageyama and R. Kanno, *J. Mater. Chem.*, 2003, **13**, 957–962.
- 9 M. J. O'Malley, H. Verweij and P. M. Woodward, *J. Solid State Chem.*, 2008, **181**, 1803–1809.
- 10 D. C. Wallace and T. M. McQueen, *Dalton Trans.*, 2015, **44**, 20344–20351.
- 11 D. C. Wallace, C. M. Brown and T. M. McQueen, *J. Solid State Chem.*, 2015, **224**, 28–35.
- 12 W. D. Johnston, R. R. Heikes and D. Sestrich, *Phys. Chem. Solids*, 1958, **7**, 1–13.
- 13 A. Kitaev, *Ann. Phys.*, 2006, **321**, 2–111.
- 14 T. Takayama, A. Kato, R. Dinnebier, J. Nuss, H. Kono, L. S. I. Veiga, G. Fabbri, D. Haskel and H. Takagi, *Phys. Rev. Lett.*, 2015, **114**, 077202.
- 15 J. Knolle, D. L. Kovrizhin, J. T. Chalker and R. Moessner, *Phys. Rev. Lett.*, 2014, **112**, 207203.
- 16 Y. Singh, S. Manni, J. Reuther, T. Berlijn, R. Thomale, W. Ku, S. Trebst and P. Gegenwart, *Phys. Rev. Lett.*, 2012, **108**, 127203.
- 17 Y. Singh and P. Gegenwart, *Phys. Rev. B: Condens. Matter*, 2010, **82**, 064412.
- 18 X. Liu, T. Berlijn, W. G. Yin, W. Ku, A. Tsvelik, Y.-J. Kim, H. Gretarsson, Y. Singh, P. Gegenwart and J. P. Hill, *Phys. Rev. B: Condens. Matter*, 2011, **83**, 220403.
- 19 S. K. Choi, R. Coldea, A. N. Kolmogorov, T. Lancaster, I. I. Mazin, S. J. Blundell, P. G. Radaelli, Y. Singh, P. Gegenwart, K. R. Choi, S. W. Cheong, P. J. Baker, C. Stock and J. Taylor, *Phys. Rev. Lett.*, 2012, **108**, 127204.
- 20 F. Ye, S. Chi, H. Cao, B. C. Chakoumakos, J. A. Fernandez-Baca, R. Custelcean, T. F. Qi, O. B. Korneta and G. Cao, *Phys. Rev. B: Condens. Matter*, 2012, **85**, 180403.



21 H. Gretarsson, J. P. Clancy, Y. Singh, P. Gegenwart, J. P. Hill, J. Kim, M. H. Upton, A. H. Said, D. Casa, T. Gog and Y.-J. Kim, *Phys. Rev. B: Condens. Matter*, 2013, **87**, 220407.

22 K. Kitagawa, T. Takayama, Y. Matsumoto, A. Kato, R. Takano, Y. Kishimoto, S. Bette, R. Dinnebier, G. Jackeli and H. Takagi, *Nature*, 2017, submitted for publication.

23 A. P. Hammersley, S. O. Svensson, M. Hanfland, A. N. Fitch and D. Hausermann, *High Pressure Res.*, 1996, **14**, 235–248.

24 *TOPAS 6.0*, Bruker AXS, 2017.

25 H. M. Rietveld, *J. Appl. Crystallogr.*, 1969, **2**, 65–71.

26 R. W. Cheary and A. Coelho, *J. Appl. Crystallogr.*, 1992, **25**, 109–121.

27 R. W. Cheary, A. A. Coelho and J. P. Cline, *J. Res. Natl. Inst. Stand. Technol.*, 2004, **109**, 1–25.

28 X. Qiu, J. W. Thompson and S. J. L. Billinge, *J. Appl. Crystallogr.*, 2004, **37**, 678–678.

29 T. Proffen and S. J. L. Billinge, *J. Appl. Crystallogr.*, 1999, **32**, 572–575.

30 C. L. Farrow, P. Juhas, J. W. Liu, D. Bryndin, E. S. Božin, J. Bloch, T. Proffen and S. J. L. Billinge, *J. Phys.: Condens. Matter*, 2007, **19**, 335219.

31 Bruker AXS, *TOPAS 6.0*, 2017.

32 B. E. Warren, *Phys. Rev.*, 1941, **59**, 693–698.

33 A. A. Coelho, *J. Appl. Crystallogr.*, 2003, **36**, 86–95.

34 G. S. Pawley, *J. Appl. Crystallogr.*, 1981, **14**, 357–361.

35 A. Kern and A. A. Coelho, *CPD Newslett.*, 2005, **32**, 43–45.

36 A. Le Bail, H. Duroy and J. L. Fourquet, *Mater. Res. Bull.*, 1988, **23**, 447–452.

37 M. M. J. Treacy, J. M. Newsam and M. W. Deem, *Proc. R. Soc. London, Ser. A*, 1991, **433**, 499–520.

38 X. Wang, J. Li, R. D. Hart, A. van Riessen and R. McDonald, *J. Appl. Crystallogr.*, 2011, **44**, 902–910.

39 S. Bette, R. E. Dinnebier and D. Freyer, *J. Appl. Crystallogr.*, 2015, **48**, 1706–1718.

40 A. Kudielka, S. Bette, R. E. Dinnebier, M. Abeykoon, C. Pietzonka and B. Harbrecht, *J. Mater. Chem. C*, 2017, **5**, 2899–2909.

41 A. A. Coelho, *J. Appl. Crystallogr.*, 2000, **33**, 899–908.

42 J. H. Roudebush, K. A. Ross and R. J. Cava, *Dalton Trans.*, 2016, **45**, 8783–8789.

43 V. Todorova, A. Leineweber, L. Kienle, V. Duppel and M. Jansen, *J. Solid State Chem.*, 2011, **184**, 1112–1119.